SolarPACES 2022, 28th International Conference on Concentrating Solar Power and Chemical Energy Systems
Power Cycles
https://doi.org/10.52825/solarpaces.v1i.660

Published: 02 Feb. 2024

Thermodynamic Modeling of a Supercritical Steam Rankine Cycle for an Integrated CSP-Nuclear System

Brian T. White[1][https://orcid.org/0000-0003-1421-2920], Ben Lindley[1][https://orcid.org/0000-0002-1015-7605], Toby Raza[1], and Michael J. Wagner[1][https://orcid.org/0000-0003-2128-4658]

[1] University of Wisconsin-Madison, USA

Abstract. Renewable technologies using solar input have varied electrical power production during periods of low solar irradiance caused by cloud coverage, seasonal changes, and time of day. Nuclear power plants can load follow, but due to low operating costs and high fixed costs, this capability is often not financially appealing. Implementing thermal energy storage (TES) within a synergistic solar and nuclear power cycle allows for storage during low demand periods and increased power production during high demand periods, effectively increasing dispatchability. In this paper, we examine the thermodynamic performance of an integrated system that includes concentrating solar power (CSP) and a lead-cooled fast reactor (LFR). These technologies are selected due to their similar operating temperatures, allowing for utilization of established TES technologies. Both the CSP and LFR system produce thermal power that is sent to a supercritical steam-Rankine cycle (SSRC). The SSRC model is designed to be implemented into a larger integrated energy system (IES) which contains multiple communicating models. The IES generates CSP and LFR heat profiles then utilizes the SSRC to output calculated metrics including power generation, heat rejection, and cycle efficiency.

Keywords: Complimentary Solar-Nuclear, Supercritical Steam-Rankine, Lead-Cooled Fast Reactor, Concentrating Solar Power, Modeling, Performance

Nomenclature

CSP	concentrating	**NTU**	number
EES	Engineering	**PWR**	pressurized
FWH	feedwater	**S2W**	salt-to-water
HPT	high	**SSRC**	supercritical
IES	integrated	**TES**	thermal
IPT	intermediate	**TTD**	terminal
LFR	lead	**UA**	conductance
LPT	Low	**W2S**	water-to-salt

1. Introduction

Despite climate-related consequences, the burning of fossil fuels for thermal or electrical generation is still prevalent due to their flexibility in responding to grid demand. Renewable energy technologies such as wind and solar photovoltaic do not inherently provide a means of energy storage and therefore are often curtailed when grid demand is low. Solar thermal technologies can more readily incorporate thermal energy storage (TES), allowing for continued production during periods of low solar irradiance and high grid demand. Nuclear energy is capable of load following (i.e., can modulate power output in response to price or demand signals on the grid),

but with high upfront fixed costs and relatively low operating and fuel costs, most nuclear plants operate at or near full capacity serving baseload demand for the grid while more flexible energy sources such as natural gas load follow. A novel solution considered in this paper combines complimentary CSP and LFR heat sources that share similar operating temperatures into a single synergistic cycle wherein the heat from the LFR and CSP can be used to generate power or can be stored in TES. This approach allows the LFR to operate at full thermal capacity while the power conversion cycle load follows, effectively increasing dispatchability.

Many studies have been conducted on combined nuclear and solar technologies in a single cycle. One study by the authors of this paper models integrated LFR and CSP with multiple configurations of a Brayton cycle [1]. This previous work examines the performance characteristics of a supercritical CO_2 Brayton recompression cycle, as opposed to a SSRC, with TES charging and discharging capabilities. Studies modeling coupled solar-nuclear technologies in a Rankine cycle often do not consider the option to charge the TES directly from the cycle. In three related studies, a small nuclear power source provides heating to the feedwater until the steam reaches saturated vapor conditions. Additional superheating and reheating is accomplished by salt-to-water heat exchangers drawing from molten salt TES tanks. Wang and Yin model and evaluate parabolic trough solar-thermal in combination with a small pressurized water reactor (PWR) [2]. Popov and Borissova design and model a hybrid CSP and small PWR [3]. An identical power cycle accompanied by waste heat desalination was considered by Wang et al. [4] for purposes of technoeconomic analysis. These three studies differ from the work presented in this paper in several important ways: (i) they do not consider the option to charge the TES via the nuclear heat source (the small PWR, in their case), (ii) they consider distinct solar thermal and nuclear technologies from this work, (iii) desalination occurs via a heat exchanger that is internal to the CSP salt cycle, and (iv) the steam-Rankine cycle is sub-critical in contrast to the SSRC design. Zhao et al. analyzed a combined solar-nuclear power system with a small modular reactor capable of charging a single tank packed-bed TES, as opposed to two tanks for cold and hot storage [5]. The packed bed TES is the exclusive provider of thermal power to the subcritical steam-Rankine cycle, while the small modular reactor and CSP do not directly exchange heat but instead act as peripheral thermal sources through TES charging.

In this paper, we model a complementary CSP and LFR SSRC, with the TES capable of `charging' and `discharging' energy on demand to increase system dispatchability. The feedwater heater (FWH) chain is comprised of four low pressure FWHs, three high pressure FWHs, and an open FWH (deaerator) with drains routed from higher to lower pressure in sequence. These eight FWHs are necessary to incrementally increase the feedwater temperature from the outlet of the condenser to the inlet requirements of the LFR steam generator. The cycle includes three turbines with a total of eight steam extraction ports that supply heat to the FWH chain. The feedwater is circulated through the cycle using a low pressure and a high-pressure pump positioned after the condenser and deaerator, respectively.

Heat is delivered to the TES system in one of two ways: (i) by heat absorbed in a CSP tower utilizing molten salt as the HTF, or (ii) by a steam-to-salt heat exchanger using a steam bypass of the first high-pressure feedwater heater. The TES discharge operation provides heated steam to the inlet of the *intermediate pressure* turbine. The LFR operates at a supercritical pressure of 330 bar which has certain advantages over subcritical systems, including increased power generation and average thermal efficiency improvement of 6%. However, reheat is typically needed to maintain turbine steam qualities above 0.90% [6]. Representative LFR operating temperatures have been provided by an industry partner and are held constant throughout this study. The heat input from the LFR is 950 MW with inlet and outlet temperatures of 340°C and 632°C, respectively. The heat input to the CSP is a constant 750 MW of thermal energy from the solar receiver, and the upper TES temperature is constrained by the decomposition temperature of solar salt (60% sodium nitrate and 40% potassium nitrate by weight), with TES hot tank at 560°C and cold tank at 350°C.

The SSRC discussed in this paper is a subsystem within in a larger system—the IES. The IES combines multiple models; LFR, CSP, electrical grid, and a multi-effect distillation process in an interacting simulation system. The SSRC model takes as input performance information from the CSP and LFR heat source models, then outputs information on heat rejection to the multi-effect distillation process and electrical generation to the grid. A diagram of the IES is illustrated in Figure 1.

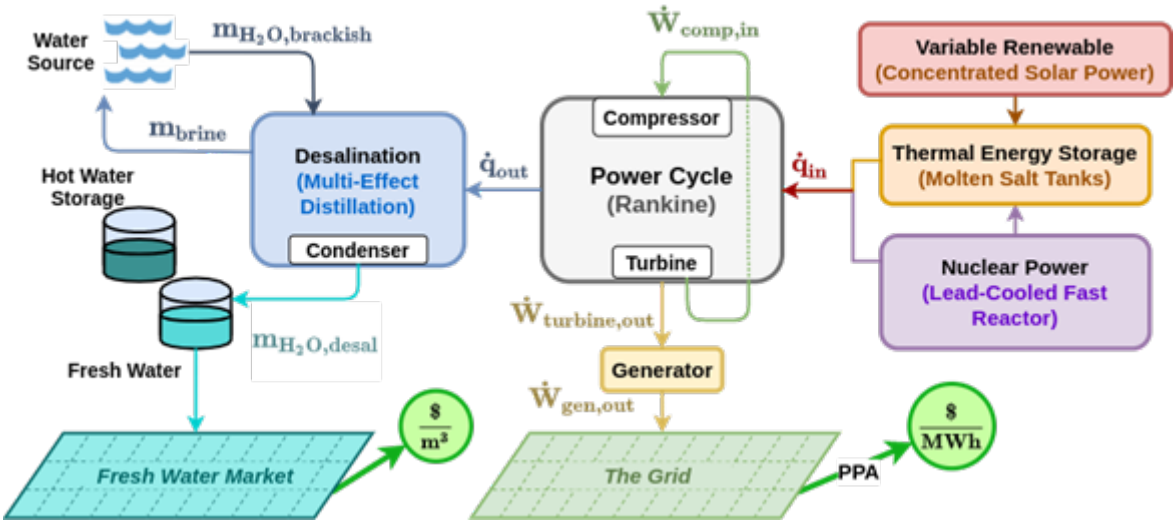

Figure 1. IES with the supercritical steam-Rankine as primary power cycle [7].

The following methodology section begins with explanations of cycle component modeling with discussion on heat exchanger model types, turbine modeling and considerations, and the SSRC with CSP integration. Methodology is followed by the study results focusing on power generation, efficiency, and design criteria for future off-design studies. Finally, closing thoughts are provided in the conclusion section.

2. Methodology

To achieve insight and a thermally accurate representation of the SSRC plus LFR and CSP technologies, a state-point model is developed in Engineering Equation Solver (EES). EES is chosen as the primary modeling software because of the integrated thermodynamic property libraries, iterative solver, and parametric study capability.

2.1. Heat Exchangers

Multiple heat exchanger modeling approaches are required to capture on-design performance metrics while considering internal phase changes and dissimilar fluid types. Depending on the situation, methodologies used for heat exchanger model include sub-heat exchanger, FWH, and simple `black box' models. The sub-heat exchanger model spatially discretizes a heat exchanger to capture more detailed behavior including local phase and capacitance rate changes. Figure 2 illustrates how a larger counter-flow heat exchanger is broken up into several (N) subsections with the inlet and outlet states of the internal sub-heat exchanger being determined by the neighboring sub-heat exchangers.

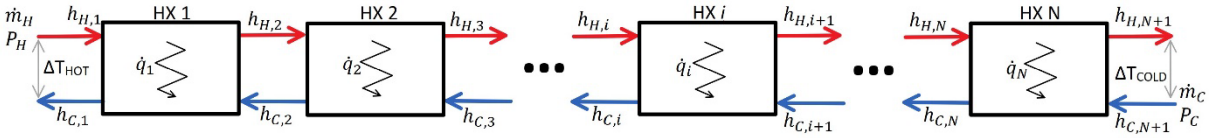

Figure 2. Sub-heat exchanger diagram for counter-flow heat exchanger with approach temperature defined.

A sub-heat exchanger model has been developed as a procedure in EES. The model takes several inputs: fluid names, mass flow rates ($\dot{m}_H$ and $\dot{m}_C$), inlet enthalpies ($h_{h,1}$ and $\mathrm{h_{C,N+1}}$), and constant pressures (P_H and P_C) for the hot and cold streams. Additionally, the number of desired heat exchanger subsections (N) and an approach temperature (ΔT) are defined.

This procedure begins by assuming an approach temperature on the "COLD" side of the counter-flow heat exchanger, which determines the outlet temperature and hence the outlet enthalpy ($h_{H,N+1}$) of the hot stream. Using an energy balance, the total heat transfer rate required to lower the hot stream to the approach temperature is calculated and evenly distributed among the N sections. The individual sub-heat exchangers are then subjected to the evenly distributed heat transfer rates ($\dot{q}_{1\ldots N}$) through an energy balance function. This process repeats the energy balance calculation for each sub-heat exchanger generating hot and cold enthalpy arrays with their associated inlet and outlet conditions.

Once the enthalpy arrays are calculated, the temperature difference on the "HOT" side is compared to the set ``COLD'' side. If the temperature difference is less than the specified approach temperature, the procedure is rerun with the approach temperature starting on the "HOT" side. This check ensures that the heat exchanger operates at the design approach temperature of 10°F (5.55°C) and does not converge to a solution consisting of a physically larger heat exchanger with a smaller approach temperature. This sub-heat exchanger model is implemented in the multi-fluid-type SALT-to-WATER (S2W) and WATER-to-SALT (W2S) heat exchangers utilizing the state point arrays to calculate design criteria such as conductance (UA), number of transfer units (NTU), and effectiveness (ε) of the heat exchangers.

The sub-heat exchanger model is capable of calculating internal state points and design criteria for counter-flow heat exchangers with multiple fluid types and phase changes. However, special considerations are required when considering a FWH in which the drains cascade backwards. In this FWH design, the flow is driven by the pressure difference between the preceding turbine, which operates at a higher temperature and pressure, and the subsequent FWH, which operates at a lower temperature and pressure. The flow responsible for this process is known as the “drain.”

The FWH with backward-drain introduces an additional inlet in each FWH, resulting in three inlets: feedwater, turbine exhaust, and drain. The turbine exhaust enters the FWH as high-temperature steam and undergoes heat exchange with the relatively colder feedwater in the desuperheater, condenser, and drain cooler regions. In the desuperheater region, the superheated turbine exhaust transfers heat to the feedwater until the flow cools to the vapor saturation temperature. If the turbine exhaust is already at the saturated vapor condition, as is the case with the low-pressure turbine, the model is configured to disable the desuperheating region calculations.

The constant temperature flow continues through the condenser region, transferring heat to the feedwater until the flow condenses into saturated liquid. The condensed turbine exhaust then mixes with the drain from the previous FWH and continues to subcool in the drain cooler region. Figure 3 provides an illustration of an individual FWH configuration within the FWH chain. It shows how the FWH is connected to the preceding and subsequent FWHs, divided into three regions (desuperheater, condenser, and drain cooler), and equipped with three inlets and a drain mixer, denoted as M.

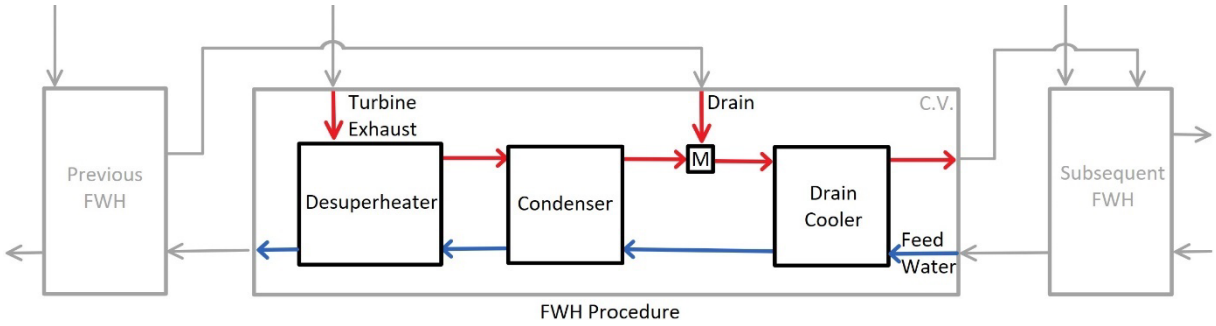

Figure 3. The subsections of a feedwater heater as modeled in EES, including the desuperheater, condenser, and drain cooler. Flow into the component includes the turbine exhaust and drain inlet on the hot side and the feedwater on the cold side.

The desuperheater, condenser, and drain cooler regions utilize the sub-heat exchanger model procedure to resolve each region's internal behavior and design point calculations. To ensure that the feedwater heater procedure does not violate the second law, the pressure on the turbine exhaust is specified using the terminal temperature difference (TTD), which is defined as the difference between the saturation temperature of the turbine exhaust and the outlet of the feedwater. The TTD is typically within a range of 0 to 3 °C and -3 to 0°C for the low and high pressure FWHs, respectively [8].

Increasing the number of subsections inside of each heat exchanger increases computation time, model complexity, and the likeliness that EES will fail to converge to a solution. Some heat exchangers, such as the LFR, CSP receiver, and the cycle condenser, can be accurately modeled without high amounts of detail using `black box' heat exchangers. `Black box' heat exchangers use a single energy balance with a heat transfer into or out of the cycle to calculate inlet and outlet state points. The open feedwater heater—assuming perfect mixing of fluids—additionally acts as a `black box' heat exchanger and is modeled using an energy balance on the drain, feedwater, and turbine exhaust inlet flows while providing feedwater to the high pressure (HP) pump.

2.2. Turbines

The power generation ($\dot{W}_{gen}$) in the SSRC is obtained by summing the work outputs of the high-pressure turbine (HPT), intermediate-pressure turbine (IPT), and low-pressure turbine (LPT). Each turbine consists of multiple stages, and their exhaust flows feed into individual FWHs, with the outlet pressures determined by the TTD values discussed earlier. The HPT and IPT are modeled using a constant isentropic efficiency approach. The inputs for this procedure include fluid name, mass flow rate, inlet enthalpy and pressure, outlet pressure, and isentropic efficiency.

However, the LPT operates in the saturated vapor region, where the presence of an excess of water droplets in steam with quality less than 90% can lead to flow-accelerated corrosion on the turbine blades and a reduction in mechanical efficiency [9]. One solution to reduce turbine moisture levels is the use of a reheat stage prior to the IPT inlet. However, due to size restrictions in the LFR in this application, implementing boiler reheat is not feasible. Other reheat variations such as moisture separator reheaters are expensive and physically large, making them economically unviable. An alternative solution is moisture drying/separation using integrated grooves in the turbine shell and hollow blades, which have been modeled and experimentally studied with up to 57% liquid separation from the steam flow [10,11]. Modeling this technology from first principles is challenging and would require computational fluid dynamics, which is beyond the scope of this research. To simplify the moisture separation in the LPT stages, it is assumed that a fraction of the liquid (70%) is removed from the steam entering the next turbine stage and drained to the turbine exhaust. By making this assumption, we do not further consider the impact of droplet-induced corrosion on plant performance or

lifetime, as it is outside of the scope of this thermodynamic analysis. A diagram of an LPT stage with liquid extraction is shown in Figure 4.

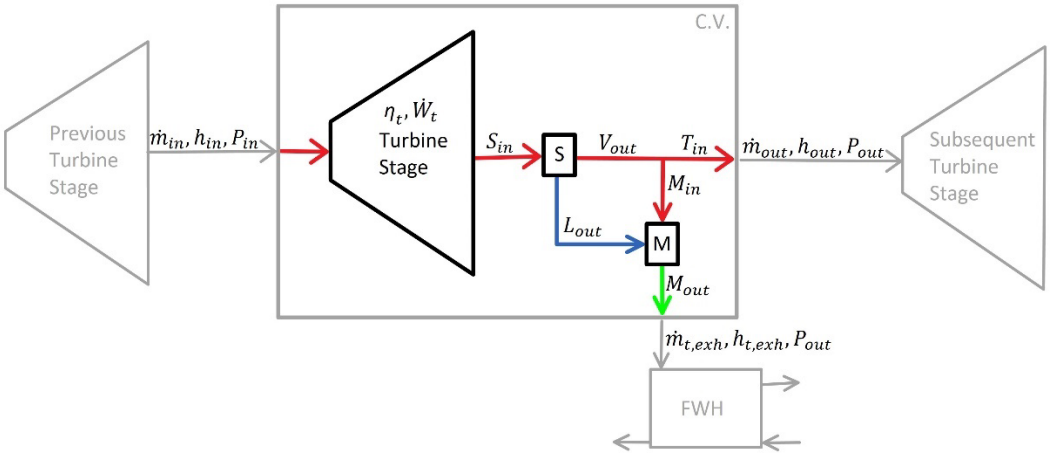

Figure 4. Low pressure turbine liquid extraction diagram with previous turbine (left) and subsequent turbine (right).

The methodology for modeling turbine behavior and moisture separation is as follows: The inlet conditions to the turbine ($\dot{m}_{in}$, h_{in}, and P_{in}) are calculated using the previous turbine stage procedure. The turbine stage operates with a specified constant isentropic efficiency (η_t) of 90%. The outlet state from the stage (S_{in}) has computes the quality, which is defined as the ratio of vapor mass to the total mass, and the vapor mass can be determined and subtracted from the total mass to obtain the liquid mass. As a result, 70% of the liquid is removed and flows to the exhaust (L_{out}), while the higher-quality steam from the moisture separation (V_{out}) flows to the subsequent turbine stage. The FWH requires a specific amount of heat input to raise the temperature of the feedwater, so a portion of the higher-quality steam (M_{in}) is combined with the extracted liquid in the mixer (M) using a simple energy balance. The combined liquid and vapor (M_{out}) serve as the turbine exhaust to the FWH, while the majority of the flow (T_{in}) serves as an input to subsequent LPT stages with qualities above 90%. The turbine procedure also provides the turbine stage work ($\dot{W}_t$), and the total turbine power generation ($\dot{W}_{HPT}$, $\dot{W}_{IPT}$, $\dot{W}_{LPT}$) is obtained by summing these internal stage work values.

2.3. Supercritical Steam-Rankine with Concentrating Solar Power

The heat inputs into the SSRC are comprised of the LFR and CSP. The CSP salt cycle contains multiple components: the receiver with heat input of 750 MW, two salt storage tanks for hot, 560°C, and cold, 350°C, TES, pumps to circulate the solar salt, and depending on the mode of operation, either charging with the W2S heat exchanger, or discharging, with the S2W heat exchanger. The CSP operates in three separate modes: `off', `charging' and `discharging'. When the CSP is in `off' mode, the LFR is the sole heat input, operating as a typical Rankine cycle with a base power output. The CSP enters `charging' mode if grid demand and price of electricity is low, storing the energy for the 'discharging' mode during high demand and price periods. When the CSP is in `charging' mode, salt is pumped from the cold tank through the W2S heat exchanger. The HPT provides high temperature and pressure steam to the W2S inlet, heating the cold salt to 560°C for storage in the hot tank. When in `discharging' mode, salt is pumped from the hot tank and exchanges heat to the SSRC until the salt temperature reaches 390°C. The cold solar salt is then stored in the cold tank. Figure 5 displays a diagram of the full SSRC.

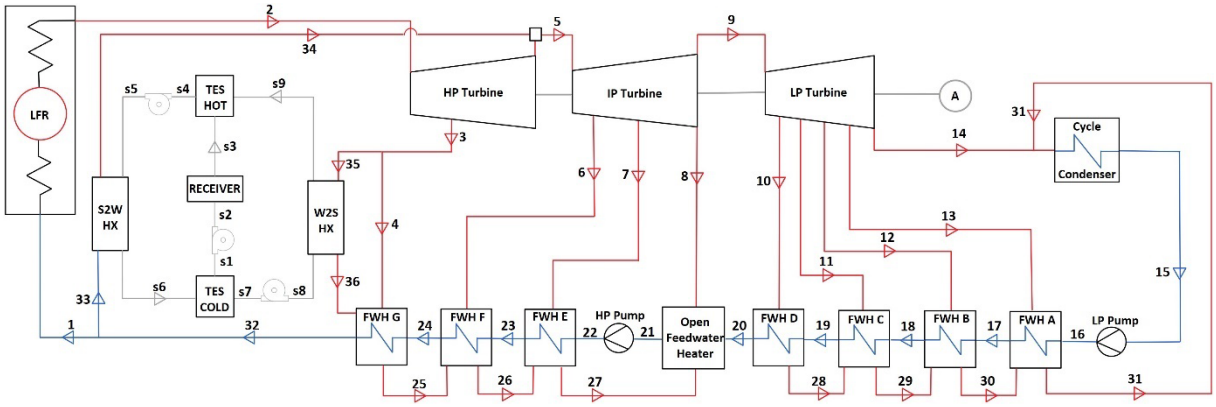

Figure 5. SSRC with complimentary LFR and CSP technologies.

The locations of the CSP W2S and S2W heat exchangers in the SSRC are constrained by the operating temperatures of the hot and cold TES. Due to the specified approach temperature of 10°C, the W2S turbine exhaust inlet must be greater than 570°C and the S2W feedwater inlet must be less than 340°C. The ideal location for the CSP W2S in charging mode utilizes supercritical exhaust from the HPT at 236.5 bar and 570°C to charge the hot TES. The outlet steam from the W2S flows to FWH G in Fig. 5, increasing the temperature of the feedwater to the required LFR inlet temperature, 340°C. In discharging mode, the S2W heat exchanger receives redirected flow from the inlet to the LFR at 330 bar and 340°C. The S2W transfers heat to the steam flow until the temperature reaches approximately 546°C, where the flow then reduces pressure through an isenthalpic valve matching properties and combining with the outlet of the HPT at state 5. The additional mass flow from the CSP in discharge mode increases the total mass flow rate through the IPT and LPT and therefore increases the total power generation output of the cycle. The efficiency of the full cycle, η_{cycle}, is calculated using Equation 1.

$$\eta_{cycle} = \frac{\dot{W}_{gen} - \dot{W}_{pump}}{\dot{Q}_{input}} = \frac{\dot{W}_{HPT} + \dot{W}_{IPT} + \dot{W}_{LPT} - \left(\dot{W}_{HP} + \dot{W}_{LP}\right)}{\dot{Q}_{LFR} + \dot{Q}_{S2W}} \quad (1)$$

Where the numerator is the total power generated by the turbines ($\dot{W}_{gen}$) minus the pump work ($\dot{W}_{pump}$). This is equivalent to the summation of the HPT ($\dot{W}_{HPT}$), IPT ($\dot{W}_{IPT}$), and LPT ($\dot{W}_{LPT}$), power outputs minus the LP pump ($\dot{W}_{LP}$) and HP pump ($\dot{W}_{HP}$) work. The denominator is the addition of heat into the cycle, where $\dot{Q}_{input}$ is the summation of the heat input from the LFR ($\dot{Q}_{LFR}$) and SALT-to-WATER ($\dot{Q}_{S2W}$) heat exchanger.

3. Results

This section presents the results of three model cases in which the cycle is evaluated in the `off', `charging' and `discharging' modes. The goal of this analysis is to highlight performance characteristics and identify challenges or benefits of cycle integration as previously described. To draw comparable results, the LFR inlet and outlet conditions, isentropic efficiencies of turbines, and outlet conditions of the LPT are specified to constant values. Additionally, the UA values for each FWH are calculated by initially setting the TTD values to 3°C during the three modes of operation. The largest FWH UA values observed across the three modes of operation are selected and set as constants due to their representation to the physical FWH sizing. In the `discharging' mode of operation the mass flow rates are the highest resulting in the largest UA values and therefore a 3°C TTD is reproduced in FWH A-F. The TTD value can be varied from the selected 3°C value with the FWH UA values changing accordingly. If the TTD value is increased, the UA values and heat transfer rate through the FWH reduce which in turn reduces the overall cycle efficiency. The TTD value can be decreased to some extent, increasing

cycle efficiency, but if the TTD is reduced drastically the heat exchangers converge to a solution which transfers heat from cold to hot, violating the 2nd Law of Thermodynamics. The TTD value of 3°C is selected with a buffer to prevent the previously described scenarios. The calculated values for FWH A-G UA and the respective TTD are listed in Table 1.

Table 1.FWH design criteria for all three charging modes of operation

On-Design Criteria	**Variable [Units]**	**Value**		
FWH approach temperature	ΔT [C]	5.55		
FWH A conductance	UA_A [MW/°C]	5.45		
FWH B conductance	UA_B [MW/°C]	5.2		
FWH C conductance	UA_C [MW/°C]	5.01		
FWH D conductance	UA_D [MW/°C]	4.87		
FWH E conductance	UA_E [MW/°C]	6.39		
FWH F conductance	UA_F [MW/°C]	5.37		
Mode-Dependent Criteria	**Variable [Units]**	*off*	*charging*	*discharging*
FWH G Conductance	UA_G [MW/°C]	1.76	2.59	2.13
FWH A TTD	TTD_A [°C]	1.46	1.09	3
FWH B TTD	TTD_B [°C]	1.52	1.16	3
FWH C TTD	TTD_C [°C]	1.58	1.2	3
FWH D TTD	TTD_D [°C]	1.65	1.3	3
FWH E TTD	TTD_E [°C]	0.3	0.85	3
FWH F TTD	TTD_F [°C]	-0.6	0.5	3

One complication and interesting result from this analysis is that FWH G does not have a TTD value because the turbine exhaust at this point is supercritical and therefore does not have a saturation pressure. Additionally, the UA value of FWH G must change according to each operating mode to resolve the cycle model. Importantly, this means that a physical system will require multiple FWH sections that are selectively activated to achieve the desired FWH G UA. The TTD values of the low pressure FWH A-D are above 1°C and the high pressure FWH E and F are below 1°C following with theory that the TTD decreases as turbine extraction temperature increases, requiring larger FWH de-superheating processes [8]. The TTD values are held constant at 3°C in `discharging' mode since this mode represents the design case with the largest required mass flow rates and, therefore, UA values. The several modes of operation correspond to what is expected for their individual use cases and have efficiencies, mass flow rates, and power output performance metrics calculated. The results from these calculations are displayed in Table 2.

Table 2. SSRC performance metrics for complimentary LFR and CSP with three modes of operation

		Value		
Performance Metrics	**Variable [Units]**	*off*	*charging*	*discharging*
Low Pressure Turbine Work	$\dot{W}_{LPT}$ [MW]	240.5	224.9	288.2
Intermediate Pressure Turbine Work	$\dot{W}_{IPT}$ [MW]	170.8	159.3	204.9
High Pressure Turbine Work	$\dot{W}_{HPT}$ [MW]	97.40	93.66	94.67
Total Power Output	$\dot{W}_{gen}$ [MW]	508.6	477.9	587.8
Condenser Heat Rejection	$\dot{Q}_{cond}$ [MW]	461.6	431.4	555.2
Maximum Mass Flow Rate	$\dot{m}_{max}$ [kg/s]	480.1	480.1	580.1
Cycle Efficiency	η_{cycle} [%]	51.41	48.18	50.36

In `discharging' mode, an additional 100 kg/s of steam is heated through the S2W heat exchanger and mixed prior to the IPT, generating 79.2 MW more power than the `off' base mode of operation. A minor decrease in efficiency of 1.05% is observed when comparing the `discharging' and `off' modes. This is mostly attributed to the increase in feedwater mass flow rate with pump power input and turbine exhaust to each FWH proportionally increasing. The `charging' mode stores heat from the LFR for later use and therefore decreases generation by 30.7 MW with a reduction in cycle efficiency of 3.23%. This loss in power is attributed to an increase in turbine exhaust to FWH G, reducing the available mass flow rate for generation in the IPT and LPT. Additionally, the cycle efficiency decreases because the energy stored—60.9 MW in the hot TES during `charging' mode—is not considered when calculating this metric. A complete tabulation of mass flow rate, $\dot{m}$, temperature, $T$, and pressure, $P$, calculated by the full SSRC model with the three modes of operation; `off', `charging', and `discharging', are tabulated in Appendix A (Table 3).

4. Conclusion

In this paper, an integrated CSP and LFR SSRC with TES charging capability is modeled, calculating design criteria and performance metrics in three modes of operation, `off', `charging' and `discharging'. The design approach is outlined, discussing the models for heat exchangers, turbines, CSP, and the full cycle. One of the important complications addressed in the paper is turbine moisture separation and FWH G. Plausible solutions to these complications are explained. The results of the study indicate that an LFR-operated SSRC achieves high efficiencies of up to 51.41% in the 'off' mode. By incorporating CSP with TES, the SSRC can enter the 'charging' mode, enabling thermal energy storage for later dispatch, albeit with reduced power production and efficiency (48.18%). Alternatively, the SSRC can enter the 'discharging' mode, resulting in greater power production and efficiencies (50.36%). Therefore, the integration of CSP and LFR into an SSRC enhances dispatchability. Future research will utilize the modeling techniques and design criteria presented in the study for conducting off-design studies.

Author contributions

B.T. White: methodology, conceptualization, investigation, validation, visualization, formal analysis, and writing – original draft. T. Raza: formal analysis, investigation. B. Lindley: project administration, conceptualization of system integration, funding acquisition, resources, supervision, and writing - review & editing. M.J. Wagner: conceptualization of power cycle modeling approach, funding acquisition, resources, supervision, and writing – original draft and review & editing.

Competing interests

The authors declare that they have no competing interests.

Funding

This work was supported by funding received from the DOE Office of Nuclear Energy’s Nuclear Energy University Program under contract number DE-NE0008988.

Acknowledgements

The authors gratefully acknowledge the contributions of Mr. Cory Stansbury of Westinghouse and Mr. Ty Neises of the National Renewable Energy Laboratory for their guidance and input.

References

1. B. T. White, M. J. Wagner, T. Neises, C. Stansbury, and B. Lindley, “Modeling of combined lead fast reactor and concentrating solar power supercritical carbon dioxide cycles to demonstrate feasibility, efficiency gains, and cost reductions,” Sustainability, vol. 13, no. 22, p. 12 428, 2021. doi: https://doi.org/10.3390/su132212428
2. G. Wang and J. Yin, “Design and exergy evaluation of a novel parabolic trough solar nuclear combined system,” Annals of Nuclear Energy, vol. 144, 2020. doi: https://doi.org/10.1016/j.anucene.2020.107573
3. D. Popov and A. Borissova, “Innovative configuration of a hybrid nuclear-solar tower power plant,” Energy, vol. 125, pp. 736–746, 2017. doi: https://doi.org/10.1016/j.energy.2017.02.147
4. G. Wang, J. Yin, J. Lin, Z. Chen, and P. Hu, “Design and economic analysis of a novel hybrid nuclear-solar complementary power system for power generation and desalination,” Applied Thermal Engineering, vol. 187, p. 116 564, 2021. doi: https://doi.org/10.1016/j.applthermaleng.2021.116564
5. B. Zhao, M. Cheng, C. Liu, and Z. Dai, “Conceptual design and preliminary performance analysis of a hybrid nuclear-solar power system with molten-salt packed-bed thermal energy storage for on-demand power supply,” Energy Conversion and Management, vol. 166, pp. 174–186, 2018. doi: https://doi.org/10.1016/j.enconman.2018.04.015
6. M. Salazar-Pereyra, R. Lugo-Leyte, A. E. Bonilla-Blancas, and H. D. Lugo-Mendez, “Thermodynamic analysis of supercritical and subcritical Rankine cycles,” in Turbo Expo: Power for Land, Sea, and Air, American Society of Mechanical Engineers, vol. 49866, 2016, V008T26A041. doi: https://doi.org/10.1115/GT2016-57814
7. G. J. Soto, U. Baker, B. White, B. Lindley, and M. Wagner, “Modeling a lead-cooled fast reactor with thermal energy storage using optimal dispatch and SAM,” Transactions of the American Nuclear Society, vol. 125, no. 2116, 2021.
8. M. M. El-Wakil, “Powerplant technology,” 1984.
9. J. Manabe, J. Kasahara, I. Fujita, and T. Kojima, “Recent moisture separator reheater design technologies,” Journal of engineering for gas turbines and power, vol. 132, no. 10, 2010. doi: https://doi.org/10.1115/1.4000612
10. H. Sato, et al. Investigation of Moisture Removal on Last Stage Stationary Blade in Actual Steam Turbine, vol. Volume 9: Oil and Gas Applications; Organic Rankine Cycle Power Systems; Steam Turbine, Turbo Expo: Power for Land, Sea, and Air, Sep. 2020. doi: https://doi.org/10.1115/GT2020-14831.
11. M. Hoznedl, et al. Separation of Water Film From Last Stage Guide Blades of 1000 MW Steam Turbine, vol. Volume 8: Microturbines, Turbochargers, and Small Turbomachines; Steam Turbines, Turbo Expo: Power for Land, Sea, and Air, Jun. 2019. doi: https://doi.org/10.1115/GT2019-90221.

Appendix A: SSRC Model State Points from 'off', 'charging', and 'discharging' with CSP

Table 3. SSRC Model State Points from 'off', 'charging', and 'discharging' with CSP

State Number	*Off*			*Charge*			*Discharge*		
	$\dot{m}$ [kg/s]	P [bar]	T [°C]	$\dot{m}$ [kg/s]	P [bar]	T [°C]	$\dot{m}$ [kg/s]	P [bar]	T [°C]
1	480.1	330	340	480.1	330	340	480.1	330	340
2	480.1	330	632	480.1	330	632	480.1	330	632
3	48.36	236.5	570	78.12	236.5	570	58.43	236.5	570
4	48.36	236.5	570	.	.	.	58.43	236.5	570
5	431.8	161.8	504	402	162.5	504.7	521.7	164.1	501
6	40.62	87.13	406.9	37.64	88.48	409.2	49.11	91.62	409.4
7	33.28	49.69	329.3	30.8	50.13	330.4	40.28	51.87	330.4
8	21.24	25.44	248.7	18.9	25.44	248.7	25.78	25.44	244.9
9	336.6	25.44	248.7	314.7	25.44	248.7	406.5	25.44	244.9
10	31.33	12.05	188.2	29.4	11.96	187.8	38.6	12.42	189.5
11	34.71	4.724	149.7	32.48	4.676	149.3	41.94	4.907	151.1
12	31.97	1.496	111.3	29.89	1.478	110.9	38.44	1.572	112.8
13	28.93	0.3524	72.84	27.05	0.3469	72.47	34.73	0.376	74.38
14	209.7	0.05	32.87	195.8	0.05	32.87	252.8	0.05	32.87
15	336.6	0.05	32.87	314.7	0.05	32.87	406.5	0.05	32.87
16	336.6	25.44	33	314.7	25.44	33	406.5	25.44	33
17	336.6	25.44	71.38	314.7	25.44	71.38	406.5	25.44	71.38
18	336.6	25.44	109.8	314.7	25.44	109.8	406.5	25.44	109.8
19	336.6	25.44	148.1	314.7	25.44	148.1	406.5	25.44	148.1
20	336.6	25.44	186.5	314.7	25.44	186.5	406.5	25.44	186.5
21	480.1	25.44	218.3	480.1	25.44	218.3	580.1	25.44	218.3
22	480.1	330	224.9	480.1	330	224.9	580.1	330	224.9
23	480.1	330	263.3	480.1	330	263.3	580.1	330	263.3
24	480.1	330	301.6	480.1	330	301.6	580.1	330	301.6
25	48.36	236.5	307.2	78.12	236.5	307.2	58.43	236.5	307.2
26	88.98	87.13	268.8	115.8	88.48	268.8	107.5	91.62	268.8
27	122.3	49.69	230.4	146.5	50.13	230.4	147.8	51.87	230.4
28	31.33	12.05	153.7	29.4	11.96	153.7	38.6	12.42	153.7
29	66.05	4.724	115.3	61.89	4.676	115.3	80.55	4.907	115.3
30	98.02	1.496	76.93	91.78	1.478	76.93	119	1.572	76.93
31	126.9	0.3524	38.55	118.8	0.3469	38.55	153.7	0.376	38.55
32	480.1	330	340	480.1	330	340	580.1	330	340
33	.	.	.	.	.	.	100	330	340
34	.	.	.	.	.	.	100	330	545.9
35	.	.	.	78.12	236.5	570	.	.	.
36	.	.	.	78.12	236.5	398.2	.	.	.
CSP	*Off*			*Charge*			*Discharge*		
s1	.	.	.	2340	30	350	2340	30	350
s2	.	.	.	2340	67.2	350	2340	67.2	350
s3	.	.	.	2340	67.2	560	2340	67.2	560
s4	.	.	.	.	.	.	525	30	560
s5	.	.	.	.	.	.	525	67.2	560
s6	.	.	.	.	.	.	525	67.2	350
s7	.	.	.	190	30	350	.	.	.
s8	.	.	.	190	67.2	350	.	.	.
s9	.	.	.	190	67.2	560	.	.	.